

Effect of torsion on the undrained limiting lateral resistance of piles in clay

Konstantinos Georgiadis¹ and Brian Sheil²

Initial submission, 29 January 2019

Revision #1, 26 April 2019

Revision #2,

Main text word count: 5697

Tables: 4

Figures: 11

¹ Dipl(Eng), MSc, DIC, PhD. Department of Civil Engineering, Aristotle Univ. of Thessaloniki, 541 24, Thessaloniki, Greece. kgeorg@civil.auth.gr.

² BE, PhD. Department of Engineering Science, University of Oxford, Parks Road, Oxford, OX1 3PJ, UK. brian.sheil@eng.ox.ac.uk.

1 **Abstract**

2 The behaviour of piles subjected to lateral loads has been explored by a number of
3 investigators over the past five decades. However, the vast majority of previous
4 literature have ignored the potential influence of additional torsional effects due to
5 horizontal eccentricities of the applied lateral loads. In this paper, an upper bound
6 mechanism and a lower bound stress field are presented for the calculation of the
7 ultimate combined torsional and lateral loads on single piles in clay. The
8 corresponding analytical upper and lower bound plasticity solutions are shown to be
9 in excellent agreement, bracketing the theoretically exact failure loads with an error of
10 less than 0.5%. Two-dimensional finite element analyses are also presented and the
11 computed ultimate loads and observed failure mechanisms are shown to compare very
12 well with the plasticity solutions. Based on the numerical results and analytical
13 solutions, failure load interaction diagrams and a simple empirical equation are
14 presented that allow the calculation of the lateral bearing capacity factor for any level
15 of applied torsion and pile-soil adhesion factor. It is demonstrated that the effect of
16 torsion can be very significant, causing reduction in lateral bearing capacity of up to
17 50% and therefore should be considered in design.

18

19 **Keywords:** Piles & piling, Bearing capacity, Torsion, Theoretical analysis, Plasticity,
20 Finite-element modelling

1. Introduction

Pile foundations are one of the most widely-adopted onshore and offshore foundation system. For structures subjected to environmental loading such as wind and waves, this commonly results in considerable lateral loads being transferred to the supporting foundations (Byrne and Houlsby, 2003). Significant displacements are often required to mobilise the ultimate lateral capacity and for this reason the focus of pile design has shifted towards serviceability limit state (Reddy and Stuedlein, 2017). However, rigorous serviceability limit state design, considering soil stiffness nonlinearity, is predicated on an accurate estimation of ultimate capacity (Sheil et al., 2018). A robust assessment of pile capacity therefore remains a key issue in the design of onshore and offshore pile foundation systems (Randolph, 2003).

The lateral capacity of a single pile in undrained soil has been the subject of a number of analytical (e.g. Murff & Hamilton, 1993; Yu et al., 2015), numerical (e.g. Brown & Shie, 1991; Yang & Jeremic, 2002; Georgiadis & Georgiadis, 2010; Zhang & Andersen, 2019), and experimental (e.g. Matlock, 1970; Brown et al. 1988; Jeanjean, 2009; Zhang et al., 2010; Nimityongskul et al., 2017) investigations. Using the upper bound theory of plasticity, Murff and Hamilton (1993) noted that although the ultimate lateral resistance of a pile in undrained soil increased with depth, it eventually reached a limiting value at a ‘critical depth’. Below the critical depth, the limiting pressure corresponds to a plane strain ‘flow-around’ failure mechanism and depends exclusively on the undrained shear strength of the soil and the pile–soil adhesion. Solutions for this flow-around limiting pressure have been proposed by Randolph and Houlsby (1984), Murff et al. (1989) and Martin and Randolph (2006).

By contrast, the potential influence of additional torsional effects, due to horizontal eccentricities of the applied lateral loads, on lateral pile capacity has largely been ignored. Herrera (2001), Hu (2003) and Hu et al. (2006) reported on the results of centrifuge tests of piles in sand subjected to various applied torsional-lateral loads. Thiyyakkandi et al. (2016, 2017) reported the results of a full-scale field testing programme to assess the behaviour of drilled shafts and jetted and grouted piles, respectively, to lateral-torsional loads. In all cases, these investigators reported that the lateral resistance is significantly reduced (up to 87%) by simultaneous application of torsion. It seems prudent, therefore, that the potential development of torsional loads, and their effect on lateral pile capacity, should be considered in design.

This paper explores the effect of torsion on the undrained limiting lateral resistance of a single pile. Plane strain conditions associated with deep flow-around failure are considered. The ultimate lateral resistance is determined using finite element analysis (FEA) for different levels of applied torsion and adhesion factor. An upper bound mechanism and a lower bound stress field are subsequently presented. Based on the numerical results and analytical solutions, failure load interaction diagrams and a simple empirical equation are presented that allow the calculation of the lateral bearing capacity factor for any level of applied torsion and pile-soil adhesion factor.

2. Problem definition

A description of the problem considered in this paper is presented in Figure 1. A pile with diameter D is considered embedded in undrained soil. The pile is either simultaneously translated with velocity v_0 and rotated with angular velocity ω_0 , or subjected to combined lateral load P and torque T per unit length of the pile,

68 depending on the type of analysis performed (displacement finite element analysis,
 69 upper bound limit analysis or lower bound limit analysis). The soil is assumed rigid –
 70 perfectly plastic in the upper and lower bound analyses and elastic – perfectly plastic
 71 in the finite element analyses. Adhesion factors α (ratio of the interface adhesion τ_i to
 72 the undrained strength of the soil mass s_u) ranging from 0 (smooth) to 1 (rough) are
 73 considered for the pile – soil interface. It is worth remarking that in the extreme case
 74 of a smooth interface ($\alpha = 0$), the pile fails by pure rotation for an infinitesimally
 75 small value of applied torque T , although it still has a lateral capacity.

76

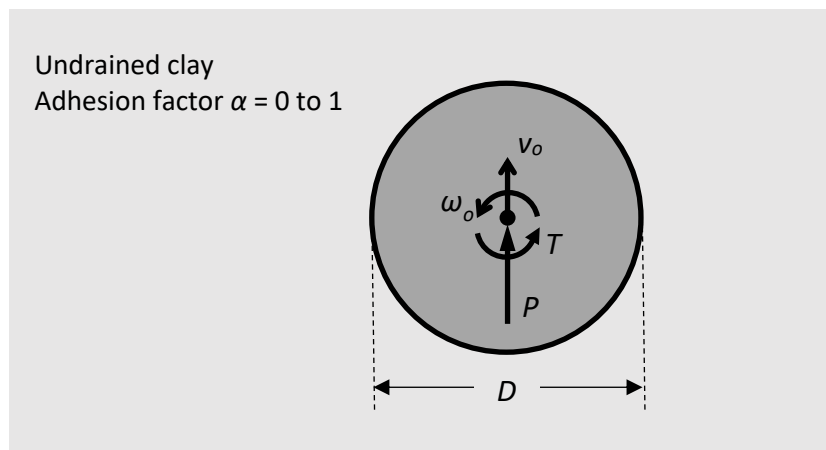
77

Table 1: Parameter normalisation adopted in this study

Variable	Dimensionless / normalised form
Lateral bearing capacity factor, N_p	$\frac{P}{s_u D}$
Torsional bearing capacity factor, N_T	$\frac{T}{s_u D^2}$
Normalised lateral load, n_p	$\frac{P}{P_u} = \frac{N_p}{N_{pu}}$
Normalised torque, n_T	$\frac{T}{T_u} = \frac{N_T}{N_{Tu}}$

78

79



80

Figure 1: Schematic plan view of a pile section embedded in undrained clay -
Definition of failure loads and associated translational and rotational velocities.
All results and discussions in this paper are presented in terms of dimensionless (N_p ,
 N_T) and normalised (n_p , n_T) loads defined in Table 1. The normalisations use the
ultimate lateral load per unit length and bearing capacity factor for purely-lateral
loading (P_u and N_{pu} respectively) and the ultimate torsional load per unit length and
bearing capacity factor for purely-torsional loading (T_u and N_{Tu} respectively).

3. Finite element analyses

3.1. Finite element mesh and material parameters

A series of plane strain FEA were performed with the finite element program
PLAXIS 2D (Brinkgreve et al. 2018) in order to determine the ultimate loads and the
associated failure mechanisms. The finite element mesh is shown in Figure 2a. It
consists of 12876 15-noded triangular elements and has dimensions 10 m \times 10 m. All
boundaries of the computational domain were restricted from movement normal to the
respective surface. A detail of the finite element mesh around the pile is shown in
Figure 2b. A total of 112 15-noded triangular elements are in contact with the pile
(520 nodes along the pile perimeter). A 1 m diameter pile was considered in all cases.
In order to apply moment loading and to ensure that the pile behaves rigidly, beam
elements with axial stiffness $EA = 15 \cdot 10^6$ kN/m and bending stiffness $EI = 5 \cdot 10^5$
kNm²/m were placed along the pile perimeter and two mutually orthogonal diameters,
as shown in Figure 2a. The soil was modelled as a weightless linear elastic – perfectly
plastic material with Tresca shear strength criterion and typical undrained soil
parameters: undrained Young's modulus $E_u = 20$ MPa, undrained Poisson's ratio $\nu_u =$
0.495 and undrained shear strength $s_u = 50$ kPa. It is worth noting that the

106 dimensionless and normalized loads presented in the following sections are
 107 independent of the selection of the above parameters. Interface elements were placed
 108 between the pile and the soil. The interface was also modelled as an elastic perfectly-
 109 plastic Tresca material with the same properties of the soil except a strength of $\tau_i =$
 110 $\alpha \cdot s_u$ was adopted.

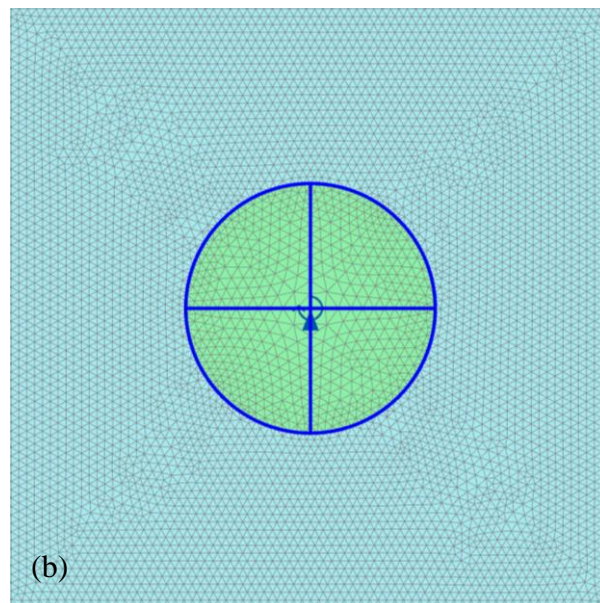
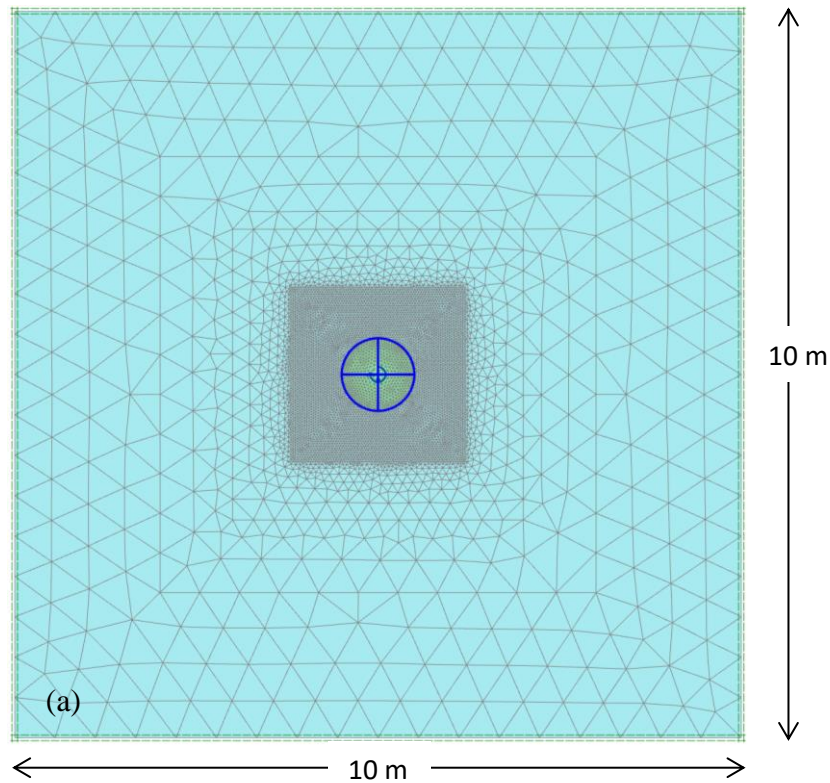


Figure 2: (a) Finite element mesh adopted for this study showing increased mesh density in zone immediately surrounding pile; 12876 elements. (b) Detail of mesh around the pile.

3.2. Finite element calculation stages

The calculation stages adopted in the finite element analyses are as follows:

1. ‘Wished in place’ installation of a weightless pile.
2. Application of a purely-torsional load, a purely-lateral load or a combination thereof until pile failure was achieved. The directions of the applied loads are shown in Figure 1.

3.3. Validation

The parameters N_{pu} and N_{Tu} were first determined by loading the pile, either laterally or torsionally, to failure for different values of α . The ultimate bearing capacity factors predicted using FEA are summarized in Table 2 and are compared with those determined analytically using:

- (a) The lower bound equation developed by Randolph and Houlsby (1984) for laterally loaded piles, which has subsequently been shown to be practically exact (Martin and Randolph, 2006):

$$N_{pu} = \pi + 2\arcsin(\alpha) + 2\cos(\arcsin(\alpha)) + 4\left[\cos\left(\frac{\arcsin(\alpha)}{2}\right) + \sin\left(\frac{\arcsin(\alpha)}{2}\right)\right] \quad (1)$$

- (b) A simple limit equilibrium calculation for purely-torsional loading:

$$N_{Tu} = \alpha \frac{\pi}{2} \quad (2)$$

It can be seen that very good agreement exists between the present FEA results and the analytical solutions.

Table 2: Ultimate bearing capacity factors for different values of α for purely-lateral or purely-torsional loading.

Adhesion factor α	Ultimate lateral bearing capacity factor N_{pu}		Ultimate torsional bearing capacity factor N_{Tu}	
	FEA	Eq. (1)	FEA	Eq. (2)
0	9.18	9.14	0	0
0.25	10.12	10.06	0.393	0.393
0.5	10.85	10.82	0.785	0.785
0.75	11.48	11.45	1.178	1.178
1	11.96	11.94	1.571	1.571

3.4. Combined lateral-torsional loading

To explore the influence of n_T on the lateral bearing capacity factor, N_p , and associated failure mechanisms, analyses were performed in which a torque was first applied to the pile followed by lateral loading to failure. The incremental displacements at failure determined for different values of the adhesion factor α (0.25, 0.5, 0.75 and 1) and normalised torque n_T (0, 0.5 and 0.95) are presented in Figure 3. For $n_T = 1$ (pure rotation), failure is confined to the pile-soil interface and is therefore not shown in this and subsequent figures. This mode of failure is the same irrespective of the value of the adhesion factor and the magnitude of lateral load. The calculated values of N_p for each case are also superimposed on the plot.

Apart from the expected loss of four-fold symmetry of the failure mechanism, the application of torque also reduces the size of the failure surface, as shown in Figure 3. The reduction in the size of the failure surface is dependent on the adopted value of α : a maximum reduction occurs for $\alpha = 1$ and is less for smaller values of α . As the lateral capacity is governed by the size of the failure mechanism, similar observations can be made for the influence of n_T on N_p . For example, an increase in n_T from 0 to

0.95 causes a reduction in N_p of 39% for $\alpha = 1$ and 9.6% for $\alpha = 0.25$. Closer inspection of Figure 3 reveals that when torque is applied, the lateral failure mechanism on the left-hand side of the pile involves a circular soil region that rotates with the pile about a point X located to the left of the pile axis. The distance between X and the centre of the pile increases as (a) α decreases and (b) n_T increases.

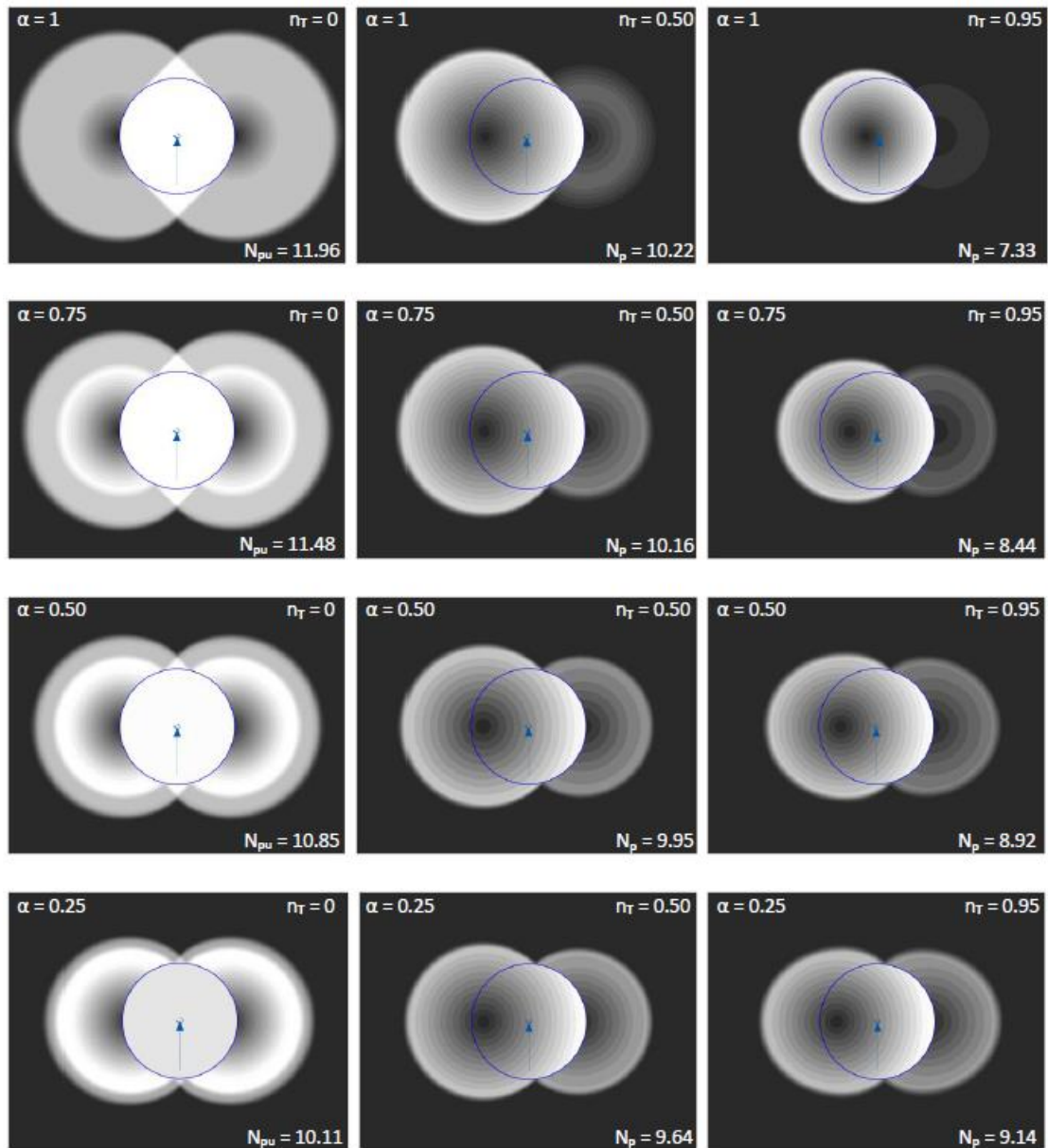


Figure 3: Contours of incremental soil displacements at failure for a laterally loaded pile with different levels of applied torsion; $\alpha = 0.25, 0.5, 0.75$ and 1.

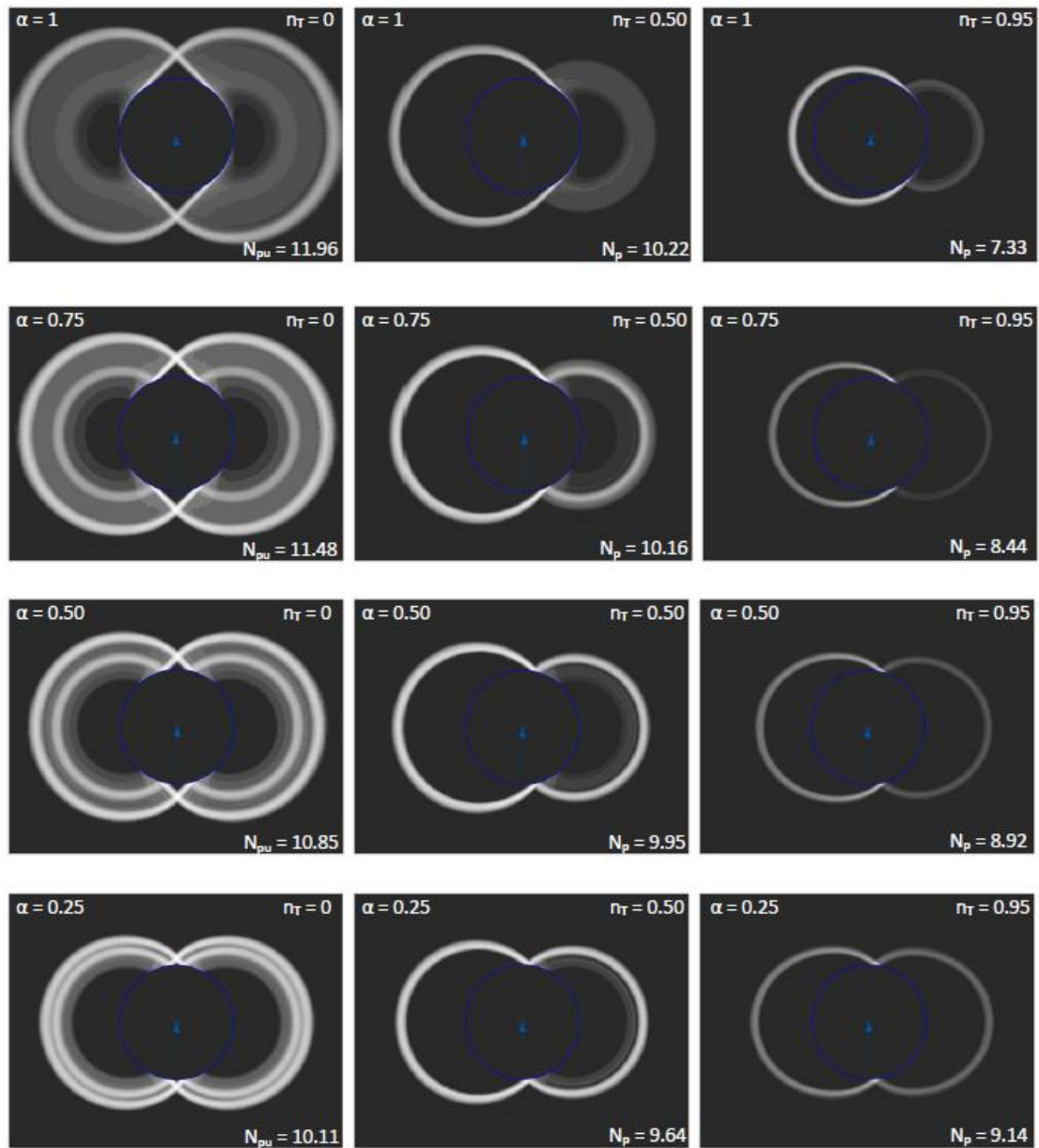


Figure 4: Contours of incremental shear strains at failure for a laterally loaded pile with different levels of applied torsion; $\alpha = 0.25, 0.5, 0.75$ and 1 .

The incremental shear strains at failure plotted in Figure 4 show that no plastic deformation occurs within this circular region of soil. Furthermore, as seen in Figure 3, no slip occurs along the section of the pile-soil interface that separates this region from the pile. It therefore follows that this soil region and the pile behave as a single rotating rigid body. The right-hand part of the mechanism involves both rigid body

rotation and shear deformation of the soil and is similar to the mechanism observed for purely lateral loading ($n_T = 0$) with one exception: there is no formation of a rigid triangular wedge at the front and back of the pile. For values of n_T close to 1 combined with small values of α , the right-hand side of the mechanism devolves into a purely rotational mechanism similar to the left-hand side.

2. Upper bound failure mechanism

Based on the failure mechanisms identified using FEA (discussed above), the mechanism shown in Figure 5 (denoted ‘Mechanism I’) is used to determine the upper bound of the ultimate lateral load, P , and torsional load, T . The mechanism is geometrically symmetrical about the horizontal axis x . The horizontal axis is also an axis of anti-symmetry with respect to velocities. On the left-hand side, the mechanism consists of a rigid body ABCHC'B'A which includes the whole pile and the soil inside the circular velocity discontinuity CHC' of radius r_x (see Figure 5). No slip takes place at the pile-soil interface segment CGC'. This rigid body rotates about point X with angular velocity ω_o , and causes the displacement and deformation of the soil on the right-hand side of the pile, as shown in Figure 5.

The right-hand side of the mechanism is based on the mechanism proposed by Martin and Randolph (2006) for a laterally loaded single pile and is similar to the mechanisms used by Georgiadis et al. (2013a,b) for laterally loaded two-pile groups and pile rows. It comprises a rigid region ABFB'A that rotates about point O and a plastically deforming region CDED'C'B'FB. While the geometry of the right-hand side of the proposed mechanism is similar to previous solutions, the velocities are different because the mode of pile movement is combined translational and rotational

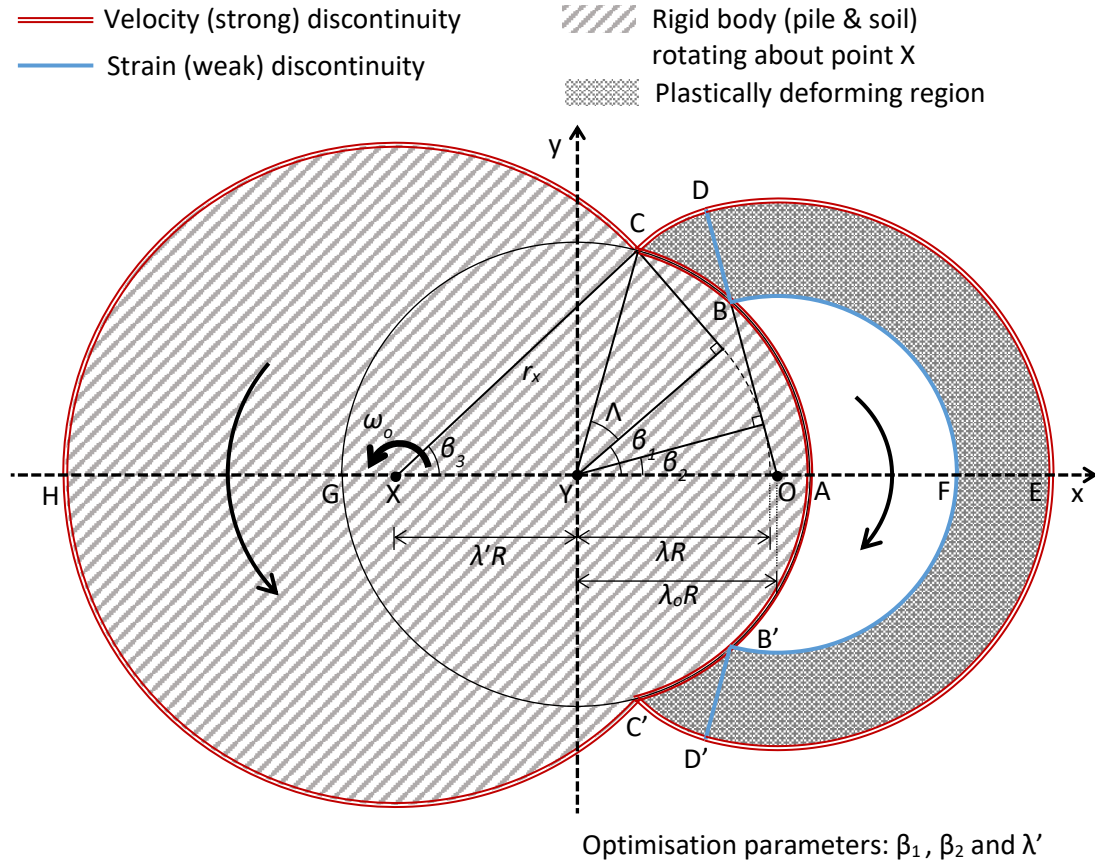


Figure 5: Upper bound failure mechanism for a pile subjected to combined lateral-torsional loading

rather than purely translational. This consequently affects the associated work calculations.

Three optimisation parameters define the geometry of the present mechanism: angles β_1 and β_2 define the extent of the right-hand part of the mechanism and the intersection points (C and C') of the two mechanisms; parameter λ' controls the position (X) of the centre of the circular velocity discontinuity CHC' and therefore the size of the rotating rigid region ABCHC'B'A. Angles β_3 and Λ , normalised distances λ and λ_o , and the radius of the left-hand part of the mechanism r_x (defined in Figure 5), can be expressed as functions of the three optimisation parameters:

$$\Lambda = \arccos(\lambda) \quad (3)$$

$$\lambda = \cos\left(\frac{\arccos(\alpha)}{2}\right) \quad (4)$$

$$\beta_3 = \arctan\left(\frac{\sin(\beta_1 + \Lambda)}{\lambda' + \cos(\beta_1 + \Lambda)}\right) \quad (5)$$

$$\lambda_o = \frac{\lambda}{\cos(\beta_2)} \quad (6)$$

$$r_x = R \frac{\sin(\beta_1 + \Lambda)}{\sin(\beta_3)} \quad (7)$$

214 The lengths of the associated velocity discontinuities can also be expressed as
 215 functions of the optimisation parameters and are presented in Table 3. The ultimate
 216 lateral load P is determined for a given T/P ratio by equating the work done by the
 217 external forces ΔW_f to the work done by the internal stresses ΔW_p . For an angular
 218 velocity ω_o of the mechanism at point X, the centre of the pile Y rotates with angular
 219 velocity ω_o and translates with velocity v_o defined as follows:

$$v_o = \omega_o \lambda' R \quad (8)$$

220 Consequently, the work done by the external forces ΔW_f can be written as:

$$\Delta W_f = v_o P \left(1 + \frac{T}{P} \cdot \frac{1}{\lambda' R}\right) \quad (9)$$

221 The work done by the internal stresses is equal to the sum of (a) the work done along
 222 each velocity discontinuity, which is a function of the velocity jump at the
 223 discontinuity, and (b) the work done within the plastically deforming regions CDB,
 224 C'D'B' and DED'B'FB, which is a function of the velocities of each region. The
 225 velocity jumps along discontinuities AB (Δv_{AB}) and BC (Δv_{BC}), and the velocities
 226 within regions CDB, C'D'B' and DED'B'FB ($v_{s,BC}$) can be obtained from the
 227 geometry of Figures 6(a) and 6(b) and are presented in Table 3 together with the

Table 3: Calculation of work done by internal stresses

Discontinuity/ region	Length	Velocity jump (Δv) or velocity (v)	Work
B'AB	$2R(\beta_2 + \Lambda)$	$v_o \left(\frac{1}{\lambda_o} + \frac{1}{\lambda'} \right)$	$2\alpha s_u R v_o \left(\frac{1}{\lambda_o} + \frac{1}{\lambda'} \right) (\beta_2 + \Lambda)$
BC and B'C'	$R(\beta_1 - \beta_2)$	$v_o \left(\frac{\cos\beta}{\lambda} + \frac{1}{\lambda'} \right)$	$2\alpha s_u R v_o \left(\frac{\sin\beta_1 - \sin\beta_2}{\lambda} + \frac{\beta_1 - \beta_2}{\lambda'} \right)$
CD and C'D'	$R(\beta_1 - \beta_2) \left[\sin\Lambda + \frac{\lambda}{2} (\beta_1 - \beta_2) \right]$	$v_o \frac{\sin(\beta_1 + \Lambda)}{\lambda}$	$2s_u R v_o \frac{\sin(\beta_1 + \Lambda)}{\lambda} (\beta_1 - \beta_2) \left[\sin\Lambda + \frac{\lambda}{2} (\beta_1 - \beta_2) \right]$
DED'	$2R \left(\frac{\pi}{2} + \beta_2 \right) [\lambda(\beta_1 - \beta_2 + \tan\beta_2) + \sin\Lambda]$	$v_o \frac{\sin(\beta_1 + \Lambda)}{\lambda}$	$2s_u R v_o \frac{\sin(\beta_1 + \Lambda)}{\lambda} \left(\frac{\pi}{2} + \beta_2 \right) [\lambda(\beta_1 - \beta_2 + \tan\beta_2) + \sin\Lambda]$
CHC'	$2R(\pi - \beta_3) \frac{\sin(\beta_1 + \Lambda)}{\sin\beta_3}$	$v_o \frac{\sin(\beta_1 + \Lambda)}{\lambda' \sin\beta_3}$	$2s_u R v_o \left(\frac{\sin(\beta_1 + \Lambda)}{\sin\beta_3} \right)^2 \frac{(\pi - \beta_3)}{\lambda'}$
BCDB and B'C'D'B'	-	$v_o \frac{\sin(\beta + \Lambda)}{\lambda}$	$2s_u R v_o \left[\sin(\beta_1 + \Lambda) \left(2 - \tan\Lambda \cdot (\beta_1 - \beta_2) - \frac{(\beta_1 - \beta_2)^2}{2} \right) \right. \\ \left. - \cos(\beta_1 + \Lambda) (\tan\Lambda + 2(\beta_1 - \beta_2)) - 2\sin(\beta_2 + \Lambda) \right. \\ \left. + \tan\Lambda \cdot \cos(\beta_2 + \Lambda) \right]$
DED'B'FBD	-	$v_o \frac{\sin(\beta + \Lambda)}{\lambda}$	$2s_u R v_o \left(\frac{\pi}{2} + \beta_2 \right) [2(\cos(\beta_2 + \Lambda) - \cos(\beta_1 + \Lambda)) \\ - \sin(\beta_1 + \Lambda)(\tan\beta_2 + \tan\Lambda + \beta_1 - \beta_2) \\ + \sin(\beta_2 + \Lambda)(\tan\beta_2 + \tan\Lambda)]$

velocity jump along discontinuity CHC' . Also presented in the same table are the work calculations for the internal stress mechanism. The upper bound estimate of the lateral bearing capacity is therefore determined by equating ΔW_f and ΔW_p ; in dimensionless form (see Table 1), this is expressed as follows:

$$N_p = \frac{2(\Delta W_p/v_o)}{s_u \left(1 + \frac{T}{P} \cdot \frac{1}{\lambda'R}\right)} \quad (10)$$

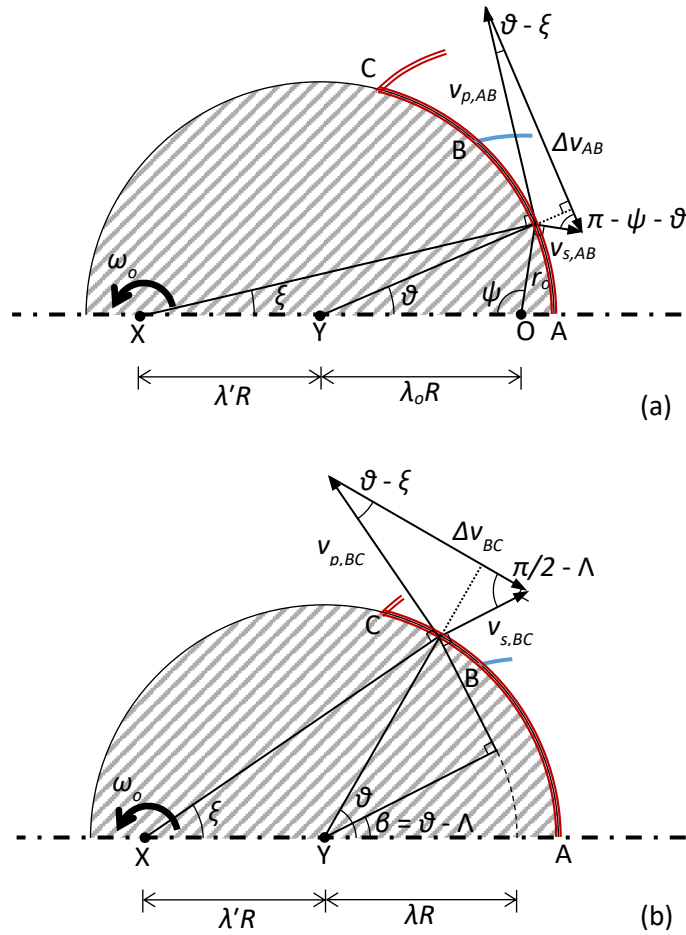
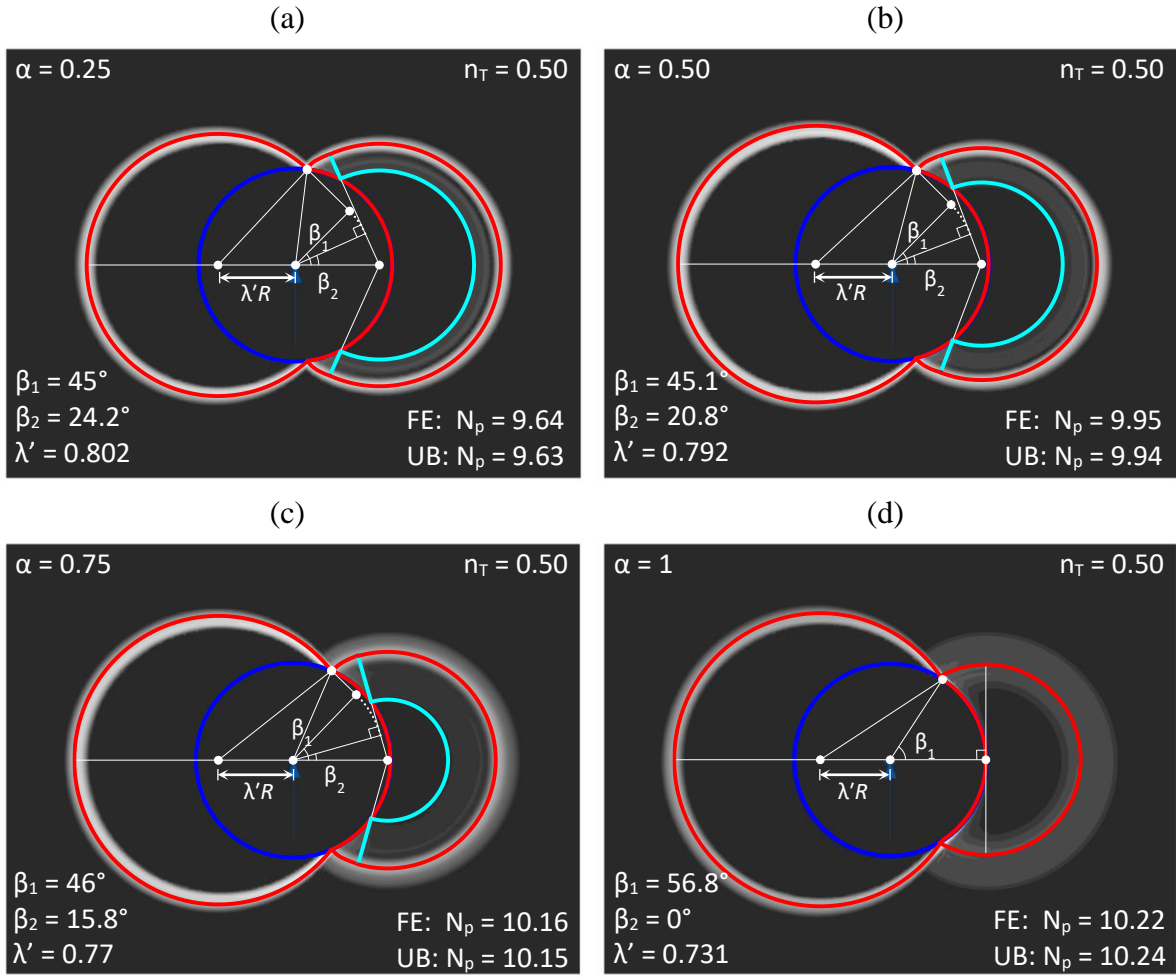


Figure 6: Calculation of velocities (v) and velocity jumps (Δv) along discontinuities (a) AB and (b) BC

Mechanism I considers no slip at the pile-soil interface on the left-hand side of the pile (CGC' in Figure 5). Slip occurs within the soil along discontinuity CHC', where the full shear strength of the soil (s_u) is mobilised. Consequently, in the limiting case when CHC' coincides with CGC' (and point X coincides with point Y in Figure 5), corresponding to pure rotation about the pile axis, Mechanism I ignores the actual value of the pile-soil adhesion factor α on the left-hand side of the pile and adopts $\alpha = 1$ instead. This is only an issue when $n_T = 1$, in which case a simple purely rotational mechanism (termed 'Mechanism II') involving a single velocity discontinuity along the pile-soil interface provides the minimum upper bound solution for N_T , given by Equation (2), which is independent of the applied lateral load. For purely-lateral loading ($n_T = 0$), Mechanism I slightly over-predicts N_p in comparison to the symmetrical Martin and Randolph (2006) mechanism. The maximum difference is 0.67%, occurring at $\alpha = 1$. Although the difference between the solutions of the two mechanisms is very small, the Martin and Randolph (2006) solution (Mechanism III) is adopted for purely-lateral loading henceforth.

In Figure 7, the optimised upper bound mechanisms for $n_T = 0.5$ and α ranging between 0.25 and 1 are compared to the incremental shear strains at failure determined using FEA. It can be seen that the optimised upper bound and FEA failure mechanisms show excellent agreement. The associated computed lateral bearing capacity factors are also in excellent agreement with a maximum discrepancy of 0.1%.



263

264 Figure 7: Comparison of incremental shear strains determined using FEA and
 265 optimum upper bound mechanisms for $n_T = 0.50$ and $\alpha =$ (a) 0.25, (b) 0.5, (c) 0.75 and
 266 (d) 1

3. Lower bound stress field

For the determination of the lower bounds of the pile failure loads, the stress field shown in Figure 8 is proposed. Similar to the upper bound analysis, a rigid rotating body consisting of the pile and a segment of the soil, is also considered here. The geometry of this rigid region is defined using optimization parameters β_0 and λ' ; the combination of these parameters that maximises the calculated failure load provides the optimum lower bound solution for each analysis. Lower bound estimates of the exact failure loads are determined using a stress field that satisfies the equilibrium equations everywhere in the domain and does not violate the failure criterion (Tresca in this case) anywhere in the domain.

The stress field around the rigid region is geometrically symmetrical about the x-x axis and therefore only the upper half of the geometry is presented. It comprises four zones: two zones on the right-hand side of the pile (Zones I and II), which are similar to the stress field used by Randolph and Houlsby (1984), a zone on the left-hand side of the pile (Zone III) and a uniform stress zone (Zone IV) that is separated from the other zones by two stress discontinuities (see Figure 8). Two sets of perpendicular stress characteristics are defined in each zone. A brief description of the stresses in the four stress zones is given below.

Zone I is a stress fan with centre A. The first set of stress characteristics in this zone are straight radial lines, as shown in Figure 8, along which the major principal stress plane angle θ_I (with respect to the horizontal plane) and the mean stress p_I are equal to:

$$\theta_I = \theta_3 + \frac{\pi}{4} \quad (11)$$

$$p_I = p_{oR} + 2s_u\theta_3 \quad (12)$$

where p_{oR} is the mean stress at $\theta_3 = 0$ (on the plane of geometrical symmetry). The second set of characteristics are circular arcs with centre at point A.

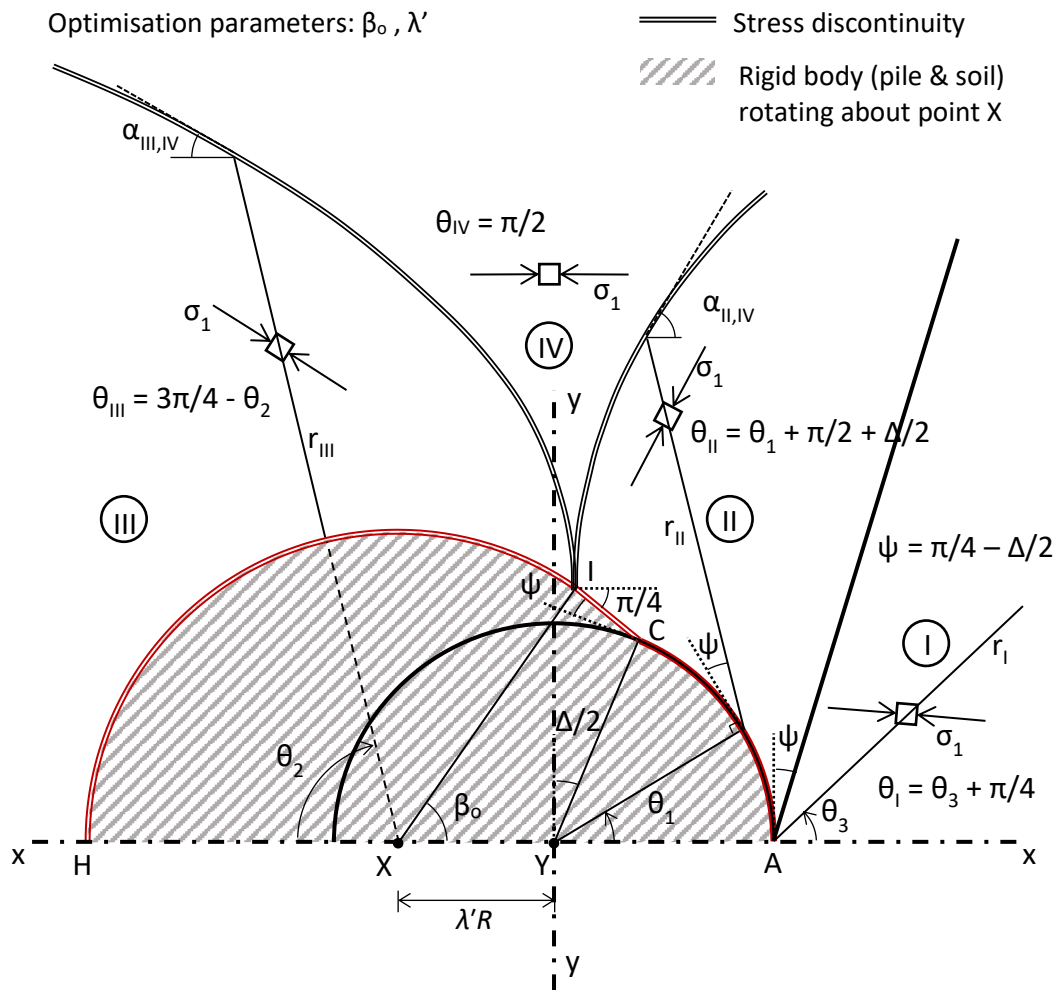


Figure 8: Lower bound stress field for a pile subjected to combined lateral-torsional loading

297 In Zone II, the first set of stress characteristics are also straight lines that intersect the
 298 pile at an angle ψ ($= \pi/4 - \Delta/2$, where $\Delta = \arcsin(\alpha)$), along which the major principal
 299 stress plane angle θ_{II} and the mean stress p_{II} are equal to:

$$\theta_{II} = \theta_1 + \frac{\pi}{2} + \frac{\Delta}{2} \quad (13)$$

$$p_{II} = p_{oR} + 2s_u \left(\theta_1 + \frac{\pi}{4} + \frac{\Delta}{2} \right) \quad (14)$$

300 In the case of a rough pile ($\alpha = 1$), the stress characteristics are tangential to the pile –
 301 soil interface ($\psi = 0$).

302 The stress characteristic at the limiting value of $\theta_{II} = \pi/2 - \Delta/2$, is inclined at $\pi/4$ to the
 303 horizontal and coincides with the straight section CI of the perimeter of the rigid region
 304 with length L_{CI} defined as follows:

$$L_{CI} = R \frac{\lambda' \sin \beta + \sin \left(\beta_o - \arccos \lambda - \frac{\pi}{4} \right)}{\sin \left(\frac{\pi}{4} + \beta_o \right)} \quad (15)$$

305 Zone III is a stress fan with centre at point X. The first set of characteristics are
 306 straight lines that extend perpendicularly from the circular perimeter of the rigid
 307 region XII, since the shear strength along this perimeter is equal to s_u . The principal
 308 stress direction and mean stresses in this region are:

$$\theta_{III} = \frac{3\pi}{4} - \theta_2 \quad (16)$$

$$p_{III} = p_{oL} + 2s_u \theta_2 \quad (17)$$

309 where p_{oL} is the mean stress at $\theta_2 = 0$ (on the plane of geometrical symmetry). The
 310 second set of characteristics are circular arcs with centre at point X and radii greater
 311 than the radius of the circular part of the rigid region, L_{XI} :

$$L_{XI} = R \frac{\lambda + \frac{\lambda'}{\sqrt{2}}}{\sin\left(\frac{\pi}{4} + \beta_o\right)} \quad (18)$$

312 Zone IV is a uniform stress zone with $\theta_{IV} = \pi/2$, the extent of which is defined by the
 313 shape and position of the two discontinuities that separate it from the other zones.

314 The lower bound estimate of the failure load is determined by first integrating the
 315 normal and shear stress components in the direction of loading (axis y-y in Figure 8),
 316 along the rigid region boundaries:

317 Boundary AC and symmetrical boundary;

$$\begin{aligned} P_{AC} = & \int_{-\left(\frac{\pi}{2}-\frac{\Delta}{2}\right)}^{\frac{\pi}{2}-\frac{\Delta}{2}} \alpha s_u R \cos \theta_1 d\theta_1 \\ & + \int_{-\left(\frac{\pi}{2}-\frac{\Delta}{2}\right)}^0 \left[p_{oR} - 2s_u \left(\frac{\pi}{4} + \frac{\Delta}{2} + \frac{\cos \Delta}{2} - \theta_1 \right) \right] R \sin \theta_1 d\theta_1 \\ & + \int_0^{\frac{\pi}{2}-\frac{\Delta}{2}} \left[p_{oR} + 2s_u \left(\frac{\pi}{4} + \frac{\Delta}{2} + \frac{\cos \Delta}{2} + \theta_1 \right) \right] R \sin \theta_1 d\theta_1 \\ & = 2s_u R \left[\frac{\pi}{2} - 1 + \Delta + \left(1 - \frac{3\pi}{2} \right) \sin \frac{\Delta}{2} + 2 \cos \frac{\Delta}{2} \left(1 + \frac{\cos \Delta}{2} \right) \right] \end{aligned} \quad (19)$$

318 Boundary CI and symmetrical boundary;

$$\begin{aligned} P_{CI} = & 2s_u L_{CI} \frac{\sqrt{2}}{2} + \left(p_{oR} + \frac{3\pi}{2} s_u \right) L_{CI} \frac{\sqrt{2}}{2} - \left(p_{oR} - \frac{3\pi}{2} s_u \right) L_{CI} \frac{\sqrt{2}}{2} \\ & = 2s_u R \frac{\lambda' \sin \beta_o + \sin \left(\beta_o - \Lambda - \frac{\pi}{4} \right) \sqrt{2}}{\sin \left(\beta_o + \frac{\pi}{4} \right)} \frac{\sqrt{2}}{2} \left(1 + \frac{3\pi}{2} \right) \end{aligned} \quad (20)$$

319

320 Boundary IH and symmetrical boundary;

$$\begin{aligned}
 P_{IH} &= \int_{-(\pi-\beta_o)}^{\pi-\beta_o} -s_u L_{XI} \cos \theta_2 d\theta_2 + \int_{-(\pi-\beta_o)}^{\pi-\beta_o} (p_{oL} + 2s_u \theta_2) \sin \theta_2 L_{XI} d\theta_2 \\
 &= 2s_u R \left(\lambda + \frac{\lambda'}{\sqrt{2}} \right) \frac{2\sin\beta_o + 2(\pi - \beta_o)\cos\beta_o - \sin\beta_o}{\sin\left(\beta_o + \frac{\pi}{4}\right)}
 \end{aligned} \tag{21}$$

321 The lower bound estimate of P (and therefore N_p) is determined by summing the
 322 forces given by Equations (19), (20) and (21):

$$N_p = \frac{P_{AC} + P_{CI} + P_{IH}}{s_u D} \tag{22}$$

323 The limiting torque T at the centre of the pile is determined by summing the
 324 components of torque acting on the boundary of the rigid region (see Figure 9):

$$\begin{aligned}
 T &= T_{AC} + T_{IH} + T_{CI} - \lambda' R (P_{CI} + P_{IH}) \\
 &= \alpha s_u R^2 (\pi - \Delta) \\
 &\quad + 2s_u L_{CI} \left[R \left(\lambda + \frac{\lambda'}{\sqrt{2}} \right) + \frac{3\pi}{2} \left(\frac{L_{CI}}{2} - L_{XI} \sin \left(\beta_o + \frac{\pi}{4} \right) \right) \right] \\
 &\quad + 2s_u (\pi - \beta_o) L_{XI}^2 - \lambda' R (P_{CI} + P_{IH})
 \end{aligned} \tag{23}$$

340 XI, IC and the pile, also do not violate the yield criterion and that the pile-soil

341 interface shear stresses are smaller than the pile-soil adhesion.

342 Following a procedure similar to that presented by Randolph and Houlsby (1984), it

343 can be shown that the stresses above the two discontinuities illustrated in Figure 8

344 also do not violate the yield criterion and therefore the solution presented above is

345 indeed a lower bound solution. The following equations are derived to determine the

346 inclinations $\alpha_{IV/I}$, $\alpha_{IV/II}$, $\alpha_{IV/III}$ and shapes of the two discontinuities:

347 Right-hand stress discontinuity between Zones IV and II ($0 < \theta_1 \leq \pi/2 - \Delta/2$):

$$r_{II} = \frac{L_{CI} - R \cos\left(\frac{\pi}{4} - \frac{\Delta}{2}\right) \left[\theta_1 - \frac{\pi}{2} + \frac{\Delta}{2} + 1 - \sin\left(\theta_1 + \frac{\Delta}{2}\right)\right]}{2 \sin^2\left(\frac{\theta_1}{2} + \frac{\Delta}{4}\right)} \quad (24)$$

$$\alpha_{IV/II} = \frac{\theta_1}{2} + \frac{\pi}{4} + \frac{\Delta}{4}$$

348 Right-hand stress discontinuity between Zones IV and I ($\theta_1 = 0$, $0 \leq \theta_3 \leq \pi/2 + \Delta/2$):

$$r_{II} = \frac{L_{CI} - R \cos\left(\frac{\pi}{4} - \frac{\Delta}{2}\right) \left[1 - \frac{\pi}{2} + \frac{\Delta}{2} - \sin\left(\frac{\Delta}{2}\right)\right]}{2 \sin^2\left(\frac{\pi}{8} - \frac{\theta_3}{2}\right)} \quad (25)$$

$$\alpha_{IV/I} = \frac{\theta_3}{2} + \frac{\pi}{8}$$

349 Left-hand stress discontinuity between Zones IV and III ($0 \leq \theta_2 \leq \pi - \beta_o$):

$$r_{III} = L_{XI} \frac{\sin^2\left(\frac{11\pi}{8} - \frac{\beta_o}{2}\right)}{\sin^2\left(\frac{7\pi}{8} + \frac{\theta_2}{2}\right)} \quad (26)$$

$$\alpha_{IV/III} = \frac{7\pi}{8} - \frac{\theta_2}{2}$$

350 Based on Equations (24) and (26), the right-hand side discontinuity at point I (Figure

351 8), where both discontinuities originate, is vertical ($\alpha_{IV/II}$ defined in Equation (24) is

equal to $\pi/2$). The left-hand side discontinuity has an inclination of $3\pi/8 + \beta_o/2$. In order to avoid overlapping of the two discontinuities, the inclination (at point I) of the left stress discontinuity must be equal to or less than $\pi/2$, which is true for any value of $\beta_o \leq \pi/4$. In fact, it can be shown that when this condition is not satisfied, a “false lower bound” solution is obtained which is greater than the upper bound solution presented in the previous section.

When $\theta_3 \rightarrow \pi/4$, r_{II} in Equation (25) tends to infinity and similarly when $\theta_2 \rightarrow \pi/4$, r_{III} in Equation (26) also tends to infinity. Therefore, the two discontinuities tend asymptotically to two lines that pass through the pile centre and are inclined at $+\pi/4$ for the right-hand side discontinuity and $-\pi/4$ for the left-hand side discontinuity.

It is straightforward to show using Mohr’s circles of stress, that the stress jump Δp at any point on a discontinuity depends on the principal stress direction jump $\Delta\theta$ at that point:

$$\Delta p = -2s_u \sin(\Delta\theta) \quad (27)$$

Using Equation (27), the vertical σ_y and horizontal σ_x stresses can be determined immediately above each discontinuity. Both σ_y and σ_x decrease monotonically along each discontinuity, from a maximum value at point I to a minimum value where the discontinuities approach their respective asymptotes. The maximum values at point I can be defined as follows:

$$\begin{aligned} \sigma_x &= p_{oR} + \left(\frac{3\pi}{2} - 1\right) s_u \\ \sigma_y &= p_{oR} + \left(\frac{3\pi}{2} - 3\right) s_u \end{aligned} \quad (28)$$

for the right-hand side discontinuity, and:

$$\begin{aligned}\sigma_x &= p_{oL} + 2 \left[\pi - \beta_o + \frac{1}{2} - \sin \left(\frac{3\pi}{4} - \beta_o \right) \right] s_u \\ \sigma_y &= p_{oL} + 2 \left[\pi - \beta_o - \frac{1}{2} - \sin \left(\frac{3\pi}{4} - \beta_o \right) \right] s_u\end{aligned}\tag{29}$$

371 for the left-hand side discontinuity. Since the stresses immediately above the
372 discontinuities must be equal at the common point I, the following relationship
373 between p_{oR} and p_{oL} is obtained by equating Equations (28) and (29):

$$p_{oR} - p_{oL} = 2s_u \left[\frac{\pi}{4} + 1 - \beta_o - \sin \left(\frac{3\pi}{4} - \beta_o \right) \right]\tag{30}$$

374 The minimum values of the stresses are obtained at $\theta_3 = \pi/4$ for the right-hand side
375 discontinuity:

$$\begin{aligned}\sigma_x &= p_{oR} + \left(\frac{\pi}{2} + 1 \right) s_u \\ \sigma_y &= p_{oR} + \left(\frac{\pi}{2} - 1 \right) s_u\end{aligned}\tag{31}$$

376 Similarly, the minimum values of the stresses are obtained at $\theta_2 = \pi/4$ for the left-hand
377 side discontinuity which can be expressed using Equation (30) as follows:

$$\begin{aligned}\sigma_x &= p_{oR} - 2s_u \left[\frac{3}{2} - \beta_o - \sin \left(\frac{3\pi}{4} - \beta_o \right) \right] \\ \sigma_y &= p_{oR} - 2s_u \left[\frac{1}{2} - \beta_o - \sin \left(\frac{3\pi}{4} - \beta_o \right) \right]\end{aligned}\tag{32}$$

378 Considering (i) a monotonic reduction of σ_x in the x-x direction from the left
379 discontinuity to the right discontinuity, (ii) that the stresses σ_y remain constant in the
380 y-y direction, and (iii) that as noted above both stresses σ_x and σ_y decrease along the
381 discontinuities from a maximum at point I, it is evident that the difference $\sigma_x - \sigma_y$ has
382 a maximum of $2s_u$ immediately above the discontinuities and is less than $2s_u$
383 everywhere else. In order to prove that the yield criterion is not violated within region

IV it needs to be demonstrated that the difference $\sigma_x - \sigma_y$ is also greater than or equal to the minimum value of $-2s_u$ everywhere in the region. From Equations (28), (31) and (32), it follows that the maximum value of σ_x in the region is given by Equation (31) (for $\theta_3 = \pi/4$) and the maximum value of σ_y is given by Equation (28) (point I in Figure 8). The minimum difference is therefore greater than $-2s_u$. Equations (28) and (31) do not apply simultaneously at any point in the region, and therefore the actual minimum difference is in fact even greater. The yield criterion is therefore not violated anywhere in the domain and the presented solution is a true lower bound solution.

4. Results and discussion

Figure 10 shows the dimensionless failure load (N_p and N_T) interaction diagram for four different values of α determined using FEA as well as the optimum upper and lower bound solutions. The FEA load interaction diagram was determined by ‘probing’, under load control, at a constant T/P ratio until failure was achieved and by first applying a predefined torque T and then lateral load P until failure. The calculated values of N_p for pertinent values of α and n_T are presented in Table 4. From both Figure 10 and Table 4, it can be seen that the three solutions are in excellent agreement for all cases. Moreover, the upper and lower bound solutions bracket the exact theoretical solutions very closely with a maximum discrepancy of less than 0.5%. For $n_T = 0$, the reader is reminded that the optimum upper and lower bound results correspond to the Martin and Randolph (2006) mechanism and the Randolph and Houlsby (1982) lower bound stress field, respectively. It is also worth remarking that since reduced pile – soil adhesion (in the case of $\alpha < 1$) is only applied to part of

the pile – soil interface in the upper and lower bound solutions of Figures 5 and 8, respectively, these solutions overestimate pure torsional failure loads. Therefore, a torsion cut-off is applied equal to the theoretical value given by Equation (2), which is in fact both an upper and a lower bound solution.

Figure 10 and Table 4 confirm that the application of torque has a significant influence on the lateral bearing capacity. This influence is greatest for $\alpha = 1$ where the maximum reduction in N_p is 50%. By contrast, the maximum reduction in N_p for $\alpha = 0.25$ is 11%. In addition, as α decreases, the value of N_p for which pile failure transitions from torsional to lateral failure also increases. To further explore the effect of α on the lateral-torsional load interaction, the results in Figure 10 are re-cast in normalised form (i.e. n_p and n_T ; see Table 1) in Figure 11. It can be seen that the lateral bearing capacity decreases as n_T increases until torsional failure takes place at a limiting n_p , equal to 0.5 in the case of $\alpha = 1$. As α decreases, the interaction diagram becomes steeper and tends to become vertical as α tends to zero. In the limiting case of $\alpha = 0$, clearly torsional failure occurs even for an infinitesimally small applied torque.

Conveniently, the failure load interaction diagram for $\alpha = 1$ is similar to a horizontal-vertical normalized load interaction diagram for a strip footing founded on undrained soil. Brinch Hansen's (1970) equation for the load inclination factor is modified here to take account of the effect of α , and transformed in terms of normalized lateral and torsional loads as follows:

$$n_p = 0.5 + 0.5\sqrt{1 - \alpha^{0.7}n_T} \quad (33)$$

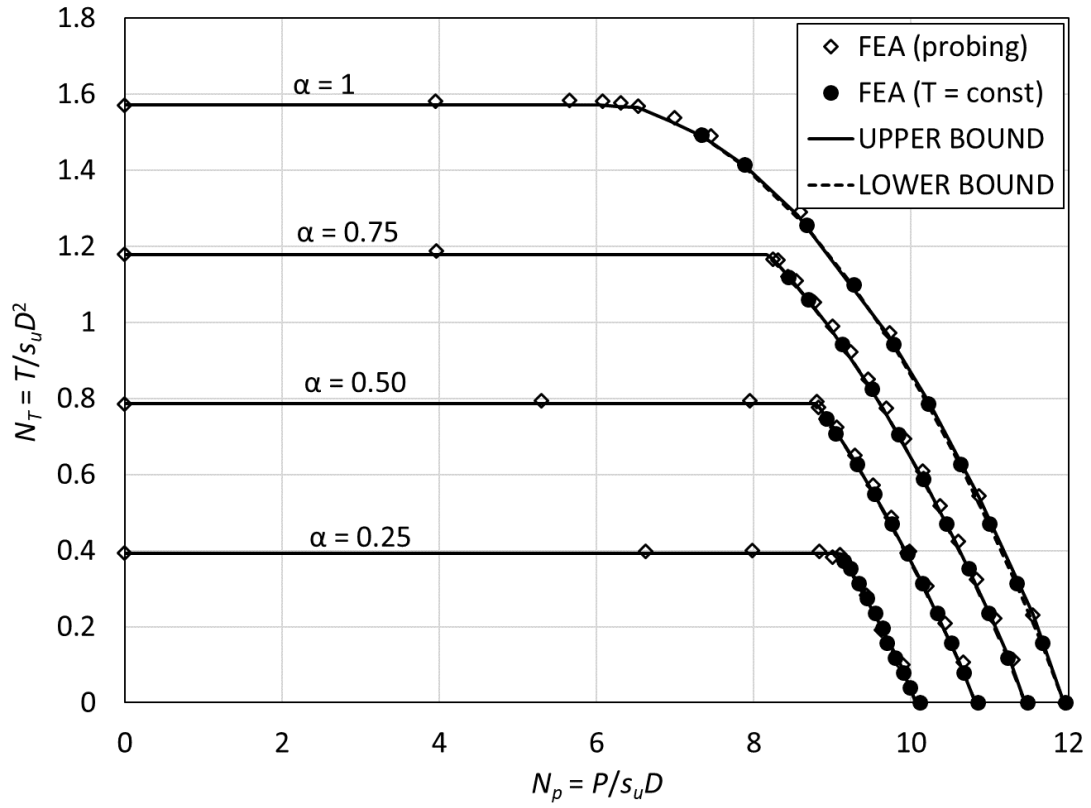


Figure 10: Dimensionless failure load interaction diagram

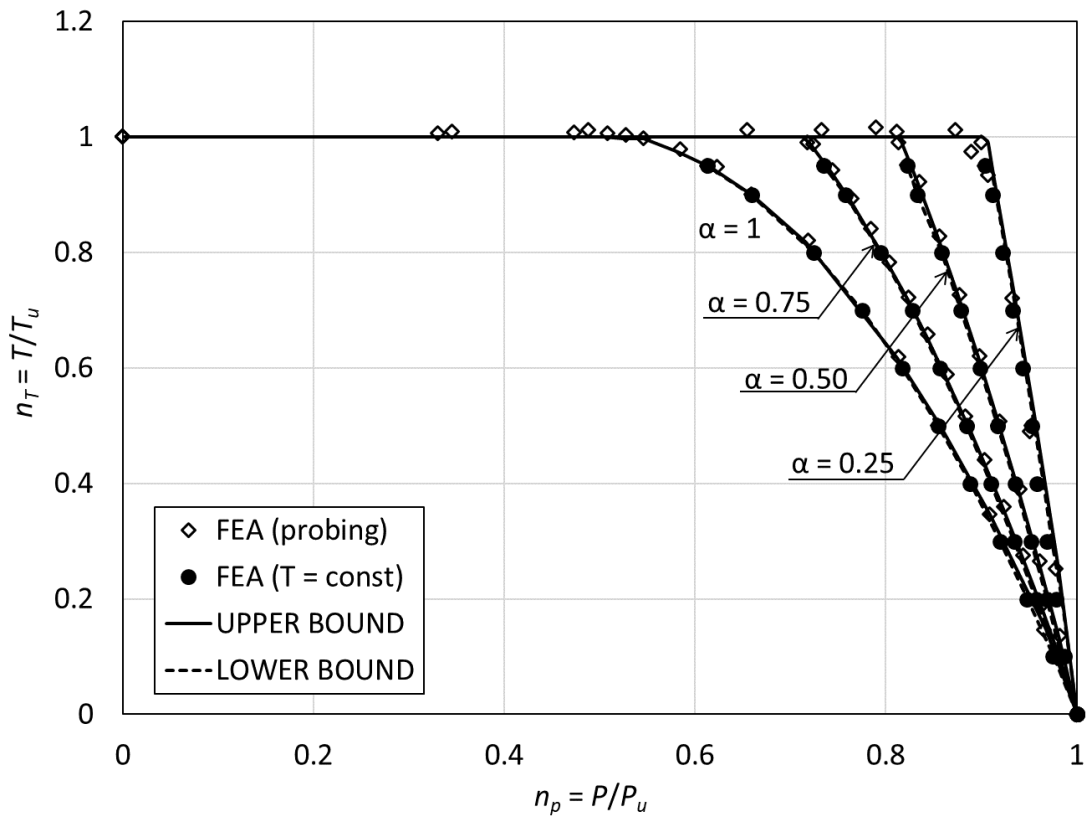


Figure 11: Normalised failure load interaction diagram

434

Table 4: Lateral bearing capacity factors N_p for different normalised torsional loads and adhesion factors

n_T	$\alpha = 1$				$\alpha = 0.75$				$\alpha = 0.50$				$\alpha = 0.25$			
	FEA	UB	LB	Eq. 33	FEA	UB	LB	Eq. 33	FEA	UB	LB	Eq. 33	FEA	UB	LB	Eq. 33
0	11.96	11.94	11.94	11.94	11.48	11.46	11.45	11.45	10.85	10.83	10.82	10.82	10.11	10.09	10.06	10.06
0.1	11.66	11.71	11.65	11.63	11.23	11.24	11.23	11.21	10.67	10.68	10.67	10.65	9.98	10.01	9.98	9.96
0.2	11.34	11.38	11.33	11.31	10.99	10.99	10.98	10.96	10.51	10.50	10.50	10.48	9.90	9.91	9.90	9.86
0.3	11.00	11.02	10.98	10.96	10.73	10.72	10.72	10.70	10.33	10.32	10.32	10.29	9.80	9.82	9.80	9.76
0.4	10.62	10.65	10.61	10.59	10.45	10.44	10.44	10.42	10.15	10.14	10.13	10.11	9.69	9.73	9.71	9.66
0.5	10.22	10.24	10.21	10.19	10.16	10.15	10.14	10.13	9.95	9.94	9.94	9.91	9.64	9.63	9.61	9.55
0.6	9.77	9.78	9.76	9.75	9.84	9.83	9.83	9.81	9.75	9.74	9.73	9.71	9.54	9.53	9.51	9.45
0.7	9.27	9.27	9.25	9.24	9.50	9.49	9.49	9.47	9.54	9.53	9.52	9.49	9.44	9.43	9.41	9.34
0.8	8.67	8.66	8.65	8.64	9.12	9.11	9.11	9.09	9.31	9.30	9.30	9.26	9.33	9.33	9.31	9.23
0.9	7.88	7.87	7.87	7.86	8.69	8.68	8.68	8.67	9.04	9.06	9.06	9.02	9.23	9.22	9.20	9.11
0.95	7.33	7.31	7.31	7.30	8.44	8.45	8.45	8.43	8.92	8.94	8.93	8.90	9.14	9.17	9.15	9.05

435

The lateral bearing capacity factors obtained using Equation (33) are compared to the FEA results as well as the upper and lower bound values in Table 4. It can be seen that this simplified equation provides an excellent approximation of the presented results.

5. Conclusions

This paper has described an investigation of the influence of torsion on the ultimate lateral capacity of a single pile wished-in-place in undrained clay. An upper bound failure mechanism and a lower bound stress field were developed that consider simultaneous translation and rotation of a pile located in an ideal rigid – perfectly plastic Tresca soil medium. The soil failure mechanisms obtained from conventional two-dimensional plane strain finite element analyses were used to inform the development of the upper bound approach. The corresponding upper and lower bound solutions were found to be in excellent agreement, bracketing the exact collapse loads with a maximum discrepancy of less than 0.5%. The failure loads obtained from the finite element analyses were also shown to be in excellent agreement with the two plasticity solutions.

Based on the numerical results and the analytical calculations, failure load interaction diagrams were presented. The diagrams revealed that torsion has a significant influence on lateral pile capacity. In the case of full adhesion ($\alpha = 1$), the application of torque was observed to reduce the lateral bearing capacity by up to 50%, before pure rotational failure occurs. This reduction is smaller for smaller values of the adhesion factor.

A simplified empirical equation was also presented for the calculation of lateral bearing capacity as a function of the applied torque. The equation is a modification of an approach for the prediction of the horizontal-vertical load interaction applied to strip footings and was calibrated through curve-fitting the results of the analyses. The empirical approach is in very good agreement with the results of all three employed methods of analysis employed in the paper.

References

- Brinkgreve, R.B.J., Kumarswamy, S., Swolfs, W.M. and Floria, F. (2018). Plaxis 2D 2018 user's manual. Plaxis B.V., Netherlands.
- Brown, D.A. and Shie, C.F. (1991). Some numerical experiments with a three dimensional finite element model of a laterally loaded pile. *Computers and Geotechnics* **12**, No. 2, 149–162.
- Brown, D.A., Morrison, C. and Reese, L.C., (1988). Lateral load behavior of pile group in sand. *Journal of Geotechnical Engineering* **114**, No. 11, 1261–1276.
- Georgiadis, K. and Georgiadis, M. (2010). Undrained lateral pile response in sloping ground. *J. Geotech. Geoenviron. Engng ASCE* **136**, No. 11, 1489–1500.
- Georgiadis, K., S. W. Sloan, and A. V. Lyamin. (2013a). Ultimate lateral pressure of two side-by-side piles in clay. *Géotechnique* **63**, No. 9, 733-745.
- Georgiadis, K., S. W. Sloan, and A. V. Lyamin. (2013b). Undrained limiting lateral soil pressure on a row of piles. *Computers and Geotechnics* **54**, 175-184.
- Brinch Hansen, J. (1970). A revised and extended formula for bearing capacity. *Danish Geotechnical Institute Bulletin* **28**, Danish Geotechnical Institute, 5-11.

482 Byrne, B.W. and Houlsby, G.T. (2003). Foundations for offshore wind
 483 turbines. *Philosophical Transactions of the Royal Society of London. Series A:*
 484 *Mathematical, Physical and Engineering Sciences*, **361**, No. 1813, 2909-2930.

485 Herrera, R. (2001). Determine optimum depths of drilled shafts subjected to combined
 486 torsion and lateral loads using the centrifuge. Master's thesis, University of Florida,
 487 Gainesville, Florida.

488 Hu, Z. (2003). *Determining the optimum depth of drilled shafts subject to combined*
 489 *torsion and lateral loads in saturated sand from centrifuge testing* (Doctoral
 490 dissertation, University of Florida).

491 Hu, Z., McVay, M., Bloomquist, D., Herrera, R., and Lai, P. (2006). Influence of
 492 torque on lateral capacity of drilled shafts in sands. *Journal of Geotechnical and*
 493 *Geoenvironmental engineering* **132**, No. 4, 454-464.

494 Jeanjean P. (2009). Re-Assessment of P-Y curves for soft clays from centrifuge
 495 testing and finite element modeling. *Proceedings of the Offshore Technology*
 496 *Conference, Houston, TX, USA*, paper OTC 20158, 1-23.

497 Martin, C.M. & Randolph, M.F. (2006). Upper bound analysis of lateral pile capacity
 498 in cohesive soil. *Géotechnique* **56**, No. 2, 141-145.

499 Matlock, H. (1970). Correlations for design of laterally loaded piles in soft clay.
 500 *Proceedings of the 2nd offshore technology conference, Houston, TX, USA*, paper
 501 OTC 1204, 577-594.

502 Murff, J.D. & Hamilton, J.M., (1993). P-ultimate for undrained analysis of laterally
 503 loaded piles. *Journal of Geotechnical Engineering*, **119**, No. 1, 91-107.

504 Nimityongskul, N., Kawamata, Y., Rayamajhi, D., & Ashford, S. A. (2017). Full-
 505 scale tests on effects of slope on lateral capacity of piles installed in cohesive soils.
 506 *Journal of Geotechnical and Geoenvironmental Engineering*, **144**, No. 1, 04017103.

507 Randolph, M.F. and Houlsby, G.T. (1984). The limiting pressure on a circular pile
 508 loaded laterally in cohesive soil. *Geotechnique* **34**, No. 4, 613-623.

509 Randolph, Mark F. (2003) Science and empiricism in pile foundation
 510 design. *Géotechnique* **53**, No. 10, 847-875.

511 Reddy, S.C. and Stuedlein, A.W. (2017). Serviceability limit state reliability-based
 512 design of augered cast-in-place piles in granular soils. *Canadian Geotechnical*
 513 *Journal* **54**, No. 12, 1704-1715.

514 Sheil, B., McCabe, B., Comodromos, E.M. and Lehane, B.M. (2018). Pile groups
 515 under axial loading: an appraisal of simplified non-linear prediction
 516 models. *Géotechnique* **69**, No. 7, DOI: 10.1680/jgeot.17.r.040.

517 Thiyyakkandi, S., McVay, M., Lai, P. and Herrera, R. (2016). Full-scale coupled
 518 torsion and lateral response of mast arm drilled shaft foundations. *Canadian*
 519 *Geotechnical Journal* **53**, No. 12, 1928-1938.

520 Thiyyakkandi, S., McVay, M., Lai, P. and Herrera, R. (2017). Suitability of jetted and
 521 grouted precast pile for supporting mast arm structures. *Canadian Geotechnical*
 522 *Journal* **54**, No. 9, 1231-1244

523 Yang, Z. and Jeremic, B. (2002). Numerical analysis of pile behaviour under lateral
 524 loads in layered elastic–plastic soils. *Int. J. Numer. Anal. Methods Geomech.* **26**,
 525 1385–1406.

526 Yu, J., Huang, M., & Zhang, C. (2015). Three-dimensional upper-bound analysis for
527 ultimate bearing capacity of laterally loaded rigid pile in undrained clay. *Canadian*
528 *Geotechnical Journal*, **52**, No. 11, 1775-1790.

529 Zhang, C., White, D., & Randolph, M. (2010). Centrifuge modeling of the cyclic
530 lateral response of a rigid pile in soft clay. *Journal of Geotechnical and*
531 *Geoenvironmental Engineering*, **137**, No. 7, 717-729.

532 Zhang, Y., & Andersen, K. H. (2019). Soil reaction curves for monopiles in clay.
533 *Marine Structures*, **65**, 94-113.

534

535

536

537

538

539 **NOTATION**

540 D : pile diameter

541 EA : axial stiffness

542 EI : bending stiffness

543 E_u : undrained modulus of elasticity

544 n_p : normalized lateral failure load per unit length

545 N_p : lateral bearing capacity factor

546 N_{pu} : ultimate lateral bearing capacity factor

547 n_T : normalized torque per unit length

548 N_T : torsional bearing capacity factor

549 N_{Tu} : ultimate torsional bearing capacity factor

550 P : lateral failure load per unit length

551 P_u : ultimate lateral failure load per unit length

552 R : pile radius

553 s_u : undrained shear strength

554 T : torque per unit length

555 T_u : ultimate torque per unit length

556 v_o : pile lateral velocity

557 $v, \Delta v$: internal velocities of failure mechanism

558 α : adhesion factor

559 $\beta_1, \beta_2, \lambda', \beta_o$: geometrical optimization parameters

560 ΔW_p : work done by internal stresses

561 ΔW_f : work done by external forces

562 ν_u : undrained Poisson's ratio

563 τ_i : pile-soil interface adhesion

564 ω_o : pile lateral velocity

565

Figure caption list

567 Figure 1: Schematic plan view of a pile section embedded in undrained clay -
568 Definition of failure loads and associated translational and rotational velocities.

569 Figure 2: (a) Finite element mesh adopted for this study showing increased mesh
570 density in zone immediately surrounding pile; 12876 elements. (b) Detail of mesh
571 around the pile.

572 Figure 3: Contours of incremental soil displacements at failure for a laterally loaded
573 pile with different levels of applied torsion; $\alpha = 0.25, 0.5, 0.75$ and 1.

574 Figure 4: Contours of incremental shear strains at failure for a laterally loaded pile
575 with different levels of applied torsion; $\alpha = 0.25, 0.5, 0.75$ and 1 .

576 Figure 5: Upper bound failure mechanism for a pile subjected to combined lateral-
577 torsional loading

578 Figure 6: Calculation of velocities (v) and velocity jumps (Δv) along discontinuities
579 (a) AB and (b) BC

580 Figure 7: Comparison of incremental shear strains determined using FEA and
581 optimum upper bound mechanisms for $n_T = 0.50$ and $\alpha =$ (a) 0.25 , (b) 0.5 , (c) 0.75 and
582 (d) 1

583 Figure 8: Lower bound stress field for a pile subjected to combined lateral-torsional
584 loading

585 Figure 9: Definition of forces and moments acting on the pile and rigid soil region,
586 and stresses acting on the boundary of the rigid region

587 Figure 10: Dimensionless failure load interaction diagram

588 Figure 11: Normalised failure load interaction diagram

589

590

591 **Table caption list**

592 Table 1: Parameter normalisation adopted in this study

593 Table 2: Ultimate bearing capacity factors for different values of α for purely-lateral
594 or purely-torsional loading.

595 Table 3: Calculation of work done by internal stresses

596 Table 4: Lateral bearing capacity factors N_p for different normalised torsional loads
597 and adhesion factors

598